International Journal of
Science and Engineering Investigations vol. 4, issue 42, July 2015
ISSN: 2251-8843

LIDAR Sensor Based Obstacle Avoidance System for Manned and Unmanned Aircraft

Roberto Sabatini[1], Subramanian Ramasamy[2], Alessandro Gardi[3]
[1,2,3]School of Aerospace, Mechanical and Manufacturing Engineering., RMIT University, Melbourne, VIC 3000, Australia
([1]roberto.sabatini@rmit.edu.au)

Abstract-The demand for reliable obstacle avoidance capabilities to ensure safe operation of manned and unmanned aircraft platforms in proximity of the terrain has led to the development of a number of obstacle detection and warning systems. Among the different technologies proposed for the application, the Light Detection and Ranging (LIDAR) technology employing eye-safe laser sources, advanced electro-optics and mechanical beam-steering components has proven to deliver the highest angular resolution and accuracy performances in a wide range of incidence angles and weather conditions. LIDAR obstacle avoidance systems have become a mature and successful solution for rotorcraft platforms, and current research activities are addressing its extension to other platforms, both civil and military. Small-to-medium size Remotely Piloted Aircraft Systems (RPAS) also employ LOAM sensor, especially for operations in proximity of the ground, further aggravated by the very limited see-and-avoid capabilities of the pilot. In this paper we describe the design and test activities performed to develop and certify the Laser Obstacle Avoidance "Marconi" (LOAM) system. After a brief description of the system architecture as well as of the data processing algorithms, emphasis is given to avoidance trajectory generation and performance estimation models. The evaluation of the avoidance trajectory generation algorithm in realistic scenario is also described. An overview of ground and flight test activities performed on various platforms and their results is also presented. The paper also overviews the future LOAM developments and integration activities with a focus on non-cooperative RPAS Detect-and-Avoid (DAA) applications.

Keywords-*Laser Sensor, Obstacle avoidance, Sense-and-Avoid, RPAS*

I. INTRODUCTION

A number of manned and unmanned aircraft missions involve low-level flight activities beyond the relatively safe aerodrome perimeter. Low level and terrain-following operations are challenged by a variety of natural and man-made obstacles, and the significant number of obstacle strike accidents recorded is a major concern both for aircraft operators and for people on the ground. Reduced atmospheric visibility due to adverse weather is frequently a contributing factor in such accidents, but the very difficult identification of small size obstacles such as wires has led to analogous accidents even in clear sky conditions. While the development of an integrated and certified Detect-and-Avoid (DAA) solution is an essential milestone for the non-segregated operation of Remotely Piloted Aircraft Systems (RPAS), significant development activities are specifically addressing the integration of obstacle detection and avoidance systems based on the technology introduced for rotorcraft [1-7]. Table 1 compares various candidate sensor technologies for Obstacle Warning System (OWS) applications in low dynamics platforms such as most rotorcraft and small RPAS. Unfortunately, state-of-the-art radar is not capable of detecting small natural and man-made obstacles such as trees, power line cables and poles. The outstanding angular resolution and accuracy characteristics of Light Detection and Ranging (LIDAR), coupled to its good detection performance in a wide range of incidence angles and weather conditions provide an ideal solution for obstacle detection and avoidance. The first experiments towards the development of a laser OWS back in 1965 employed a Nd:YAG laser [8]. Semiconductor lasers, including GaAs and GaAlAs, operating in the spectral region of 0.84 to 0.9 μm have been experimentally evaluated since 1966 [9]. The experience gained at those stages highlighted many aspects that are now acknowledged in state-of-the-art designs. Due to eye-safety and adverse weather (fog) propagation concerns, further development with Nd:YAG and various semiconductor lasers has been substantially reduced, in favour of CO_2 lasers [10, 11]. One of the first heterodyne detection CO_2 systems was the LOWTAS, developed by UTRC. More recent developments include CLARA, the Anglo-French compact LIDAR demonstrator program [12], HIWA, a German system built and tested by Eltro and Dornier [13], and OASYS, developed in the U.S. by Northrop [14]. More recent research efforts have concentrated on 1.54 μm (frequency-shifted Nd:YAG and Er:glass) solid state lasers. In the early 2000's, an eye-safe 1.54 μm system, called LOAM (Laser Obstacle Avoidance "Marconi") was developed and tested by SELEX-ES in collaboration with the Italian Air Force Flight Test Centre [15]. The LOAM is a low-weight/volume navigation aid system for rotary-wing/RPAS platform specifically designed to detect potentially dangerous obstacle placed in or nearby the flight trajectory and to warn the crew in suitable time to implement effective avoiding manoeuvres. Figure 1 depicts the LOAM in a low-level integration layout, including ad-hoc control panel and display unit combination

(i.e., no interface with other visual/FLIR sensors).The LOAM prototype was tested in 2002 both on the ground and in flight, demonstrating positive results in terms of obstacle classification and detection range [15]. The system was subsequently integrated on various rotorcraft in service with the Italian Air Force and other NATO defence forces. More recent research activities are addressing the scalability of LOAM for small size RPAS, with a special focus on the potential contributions that this LIDAR technology can provide to the development of a cost-effective integrated sensor system for non-cooperative DAA.

TABLE I. CANDIDATE OBSTACLE DETECTION TECHNOLOGIES FOR LOW-DYNAMICS PLATFORMS.

REQUIREMENT	MAGNETIC	THERMAL	MILLIMETRIC WAVE RADAR	LIDAR
Wire detection	Only energized wires	Only energized wires	All wires preferably perpendicular to flight trajectory	All wires
Detection range	Short	Short	As required	As required
Coverage Area	Small	As required	As required	As required
Resolution and accuracy (obstacle type, position and distance)	Insufficient	Good for position and type, no ranging capabilities	Medium	Very high
All-weather performance in low-level flight	Good	Poor	Very Good	Good*
False alarm rate	High	Low	Very low	Very low
Base technology status	Mature	Mature	State-of-art	State-of-art
* Laser energy is significantly attenuated by rain and blocked by clouds and fog.				

Figure 1. LOAM low-level integration on an AB-212 rotorcraft [16].

II. OPERATIONAL REQUIREMENTS

The operational requirements for a reliable and effective OWS are the following:

- Capability to detect all types of hazardous obstacles, including topographic features, vegetation, buildings, poles/masts, towers, cables and transmission lines;
- High minimum detection range, adequate for the platform airspeed performances;
- Wide Field of View (FOV), adequate for the manoeuvring envelope limits of the platform;
- High range and bearing resolutions and accuracies and good probability of detection, since no real obstacle threat shall remain undetected;
- Operability in all-weather conditions, night-time and darkness;
- Very Low False Alarm Rate, to prevent spurious warnings that would increase the crew's workload and prompt unnecessary avoidance manoeuvres, potentially disruptive to the mission safety;
- Satisfactory technological maturity levels.

III. SYSTEM DESCRIPTION

The LOAM was designed to detect obstacles placed in or nearby the aircraft trajectory, classify/prioritise the detected obstacles, and provide obstacle visual and aural warnings and information to the crew. The LIDAR beam scans periodically the area around the host platform's longitudinal axis within a FOV of 40° in azimuth and 30° in elevation. As shown in Figure 2, in order to enhance the coverage during turning manoeuvres at high yawing rates, the flight crew may select the azimuth orientation of the LOAM FOV can be tilted by 20° left/right with respect to the axis.

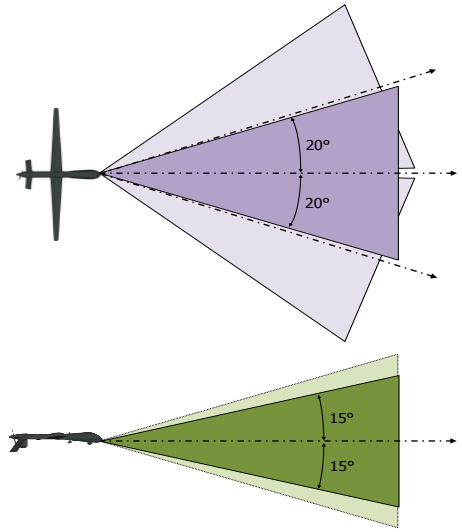

Figure 2. LOAM FOV, including lateral tilting [17].

As conceptually exemplified in Figure 3, during every full FOV scan (4 Hz refresh frequency) the LIDAR beam performs a number of elliptical scan patterns across the FOV. This scanning pattern is well suited to detect the most dangerous obstacles, like wires, due to the several and regularly spaced vertical lines that it produces. The electro-mechanical device responsible for the described scanning pattern is a swashing mirror, documented in [18]. The LOAM Er:fiber laser sub-system is the IRE POLUS model ELPM-20K, whose main characteristics are listed in Table 1.

TABLE II. ELPM-20K LASER PARAMETERS [4].

Parameter	Value
Emission wavelength	1.55μm
Pulse power at the assembly output	10 kW
Pulse Duration	2.8 ns
Pulse Repetition Frequency	40 kHz

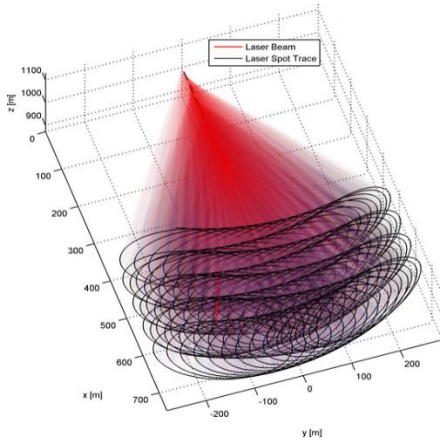

Figure 3. LOAM scan pattern for a slowly advancing platform.

IV. OBSTACLE DETECTION AND CLASSIFICATION SOFTWARE ARCHITECTURE

The signal pre-processing steps involve an analogue optical-electrical conversion of the echo signal by an Avalanche PhotoDiode (APD), a signal pre-amplification by an automatic controlled gain amplifier and a threshold comparison with adjustable threshold in order to adjust the sensitivity on the basis of the expected return signal power in relation with the time elapsed from the LIDAR pulse emission. The threshold level may also be adjusted to take into account the background conditions. These features reduce the probability of false echo detection due to the atmospheric back-scatter near the laser beam output and optimise the system sensitivity in various operational weather conditions. Subsequently, a digital signal processing is performed in order to validate positive echo detections, determine the position of the detected obstacles and their geometrical characteristics. For this purpose, the LOAM software architecture is organised in two sequential stages: Low Level Processing (LLP) and High Level Processing (HLP). Figure 4 represents the signal processing software architecture and the integrated architectures for manned and unmanned aircraft are shown in Figure 5 and 6 respectively.

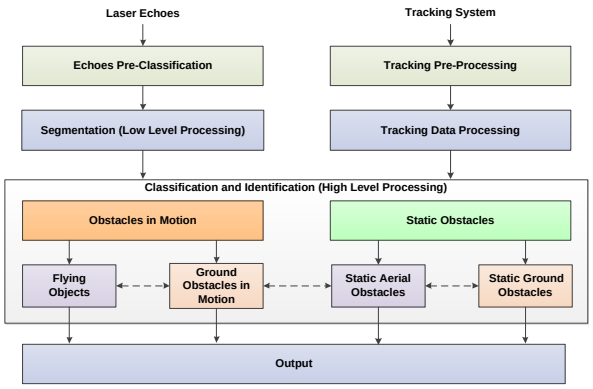

Figure 4. LOAM signal processing software architecture [17].

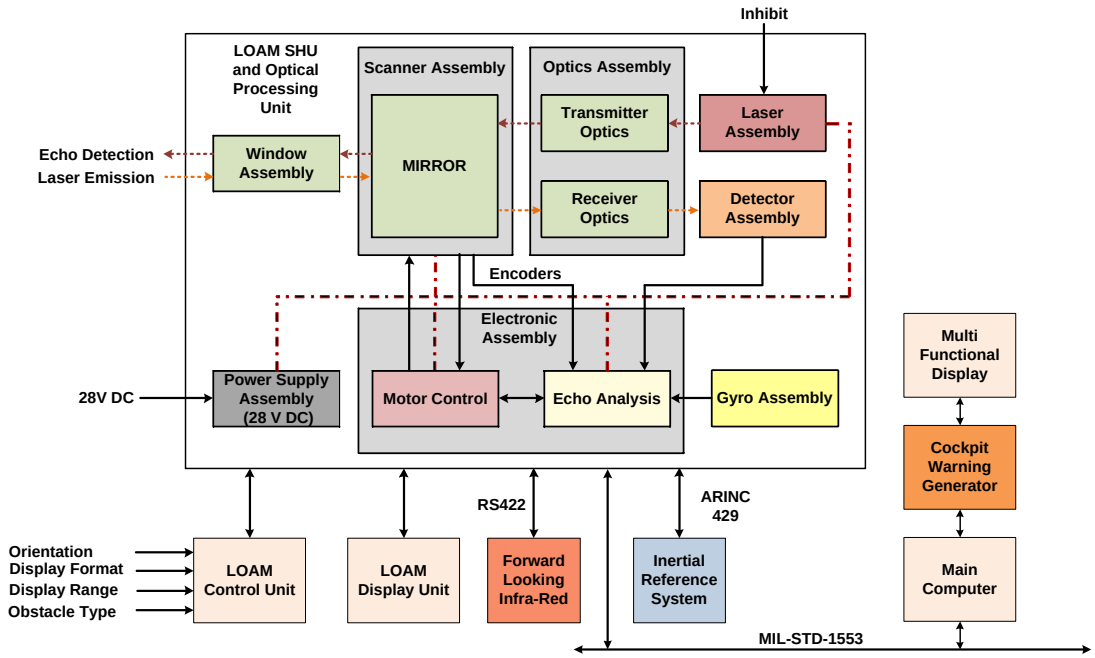

Figure 5. Architecture of the LOAM avionic integration – Manned aircraft [16].

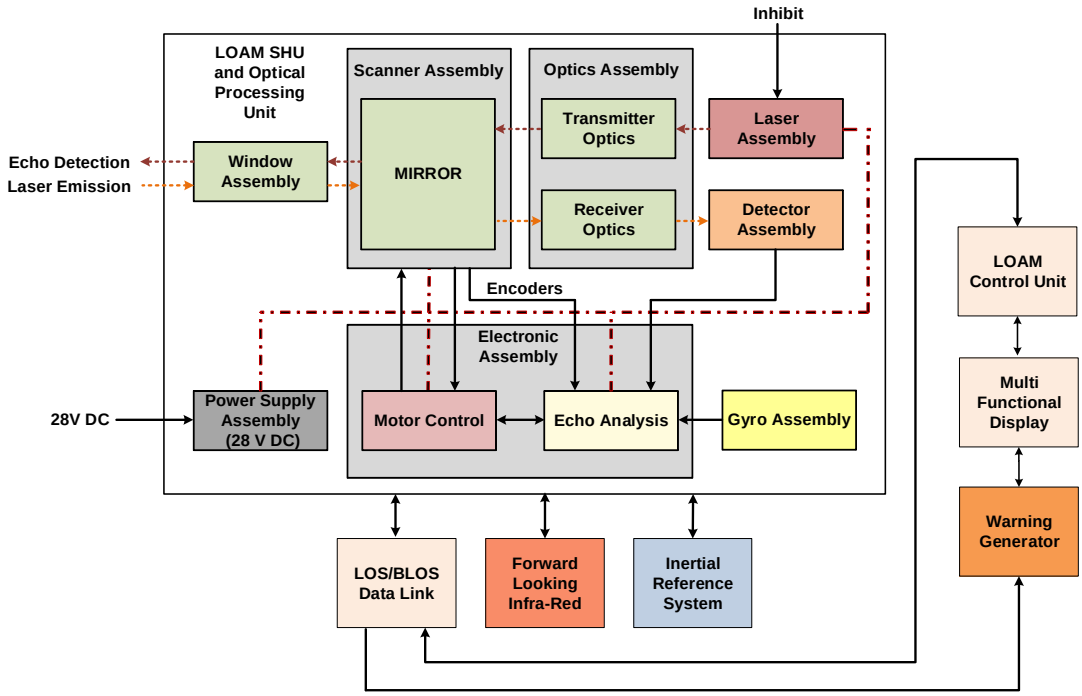

Figure 6. Architecture of the LOAM avionic integration – Unmanned aircraft [16].

The LLP is performed on the individual echoes in order to determine range, angular coordinates and characteristics of the obstacle portion generating them. The HLP analyses the LLP output to identify groups of echoes, in order to reconstruct the shape and type of the obstacle. The LOAM is capable to automatically classify obstacles according to the following classes:

- **Wire:** all thin obstacles like wires and cables (e.g., telecommunication/power lines and cableways);
- **Tree:** vertical obstacles of reduced frontal dimensions (e.g., trees, poles and pylons);
- **Structure:** extended obstacles (e.g., bridges, buildings and hills).

The wire LLP algorithm processes only the echoes whose magnitude is weaker than pre-defined thresholds. The single echoes are processed as soon as they are acquired. Subsequently, the wire HLP algorithm works on the subset of acquired echoes in the current frame. Clusters are merged into a single obstacle by means of iterative image segmentation, specifically implemented to identify echoes characterised by uniform range. A statistical algorithm subsequently validates the merged echoes by verifying if the obstacle is generated by real aligned echoes or by noise data. The processing algorithms for extended obstacles (Trees and Structures) are also divided in two different phases: echoes analysis and segmentation. The echoes already classified as extended object need to be processed by a dedicated validation algorithm, since many of these are not generated by obstacles (like, for example, the ground). A well-defined number of echoes, acquired in a short time range, have some geometrical characteristics. The segmentation algorithm is responsible of detecting, merging and validating the clusters of echoes. The LOAM performs automatic prioritisation of the detected obstacles in function of the risk represented according to the relevant range, and provides timely visual and aural warnings to the flight crew, including information of the detected obstacles. The dedicated signal processing algorithms grant reliable detection performance, independent from the platform motion, allowing a reconstruction of the obstacle shape without using navigation data (stand-alone integration) in slow-moving platforms with a benign attitude envelope. The LOAM can also be integrated with the navigation system to grant equally efficient reliable detection in extreme flight envelopes of high-dynamics platforms [4, 15]. A history function is implemented to retain obstacles information even when they are outside the FOV. Such history function stores the obstacle position and characteristics for a defined time and updates it based on the platform motion. Since both the obstacle data and the platform navigation data are affected by errors, a propagation of uncertainty is performed to grant a minimum 95% confidence level (2-sigma) to obstacle positions.

V. Calculation of Avoidance Trajectories

Once the obstacle has been detected, classified and prioritised as described, LOAM triggers the generation of feasible avoidance trajectories based on the platform dynamics, obstacle positions and shapes. An optimal avoidance trajectory is subsequently identified among the feasible set based on a robust multi-criteria decision logic. The original avoidance trajectories generation algorithm for rotorcraft platforms was introduced in [4]. Similarly to the rotorcraft case, the 4D avoidance trajectory generation algorithm for fixed-wing aircraft follows the dynamic programming approach. A direct optimisation method is adopted, hence the algorithm is based on the aircraft dynamics, and not on a geometric trajectory model.

5.1 Fixed-wing flight dynamics model

The approximated dynamic model of the fixed-wing aircraft for avoidance trajectory generation by the LOAM is derived by introducing the following assumption [17]:

- The aircraft is modelled as a point-mass rigid body with three linear degrees of freedom (3DOF);
- The mass of the aircraft is considered constant along the avoidance trajectory;
- The inertial reference system adopted is centred on the initial aircraft position, with the X axis pointing eastward, the Y axis northward and the Z axis normal to the ground;
- The aircraft is subject to a constant gravitational acceleration parallel and opposite to the Z axis, and for the purpose of our estimation we assume $g = 9.81\ m/s^2$;
- The airspeed is expressed as True Air Speed (TAS). In our case, the assumed initial TAS is $v = 25\ m/s$. The effects of wind are considered in the dynamics model, but not simulated.

The resulting system of differential equations for 3-DoF vehicle dynamics is:

$$\begin{cases} \dot{v}^* = \tau \cdot T^* - D^* - sin\gamma \\ \dot{\gamma} = \frac{1}{v^*} \cdot (N \cdot cos\mu - cos\gamma) \\ \dot{\chi} = \frac{1}{v^*} \cdot \frac{N \cdot sin\mu}{cos\gamma} \\ \dot{x} = v^* \cdot g \cdot cos\gamma \cdot sin\chi + v_{wx} \\ \dot{y} = v^* \cdot g \cdot cos\gamma \cdot cos\chi + v_{wy} \\ \dot{z} = v^* \cdot g \cdot sin\gamma + v_{wz} \end{cases} \quad (1)$$

where *T* is thrust, *D* is aerodynamic drag, γ is flight path angle, χ is track angle and μ is bank angle. The accuracy of 6 Degrees-of-Freedom (3-DoF) flight dynamics is shown here to be adequate for low-dynamics platforms, and in combination with smooth control logics leads to the generation of relatively smooth avoidance trajectories. Additional trajectory generation algorithms based on 6 Degrees-of-Freedom (6-DoF) dynamics are currently being developed, with aerodynamic and inertia coefficients retrieved as documented in [19].

5.2 Control logic

During the avoidance manoeuvre, the load factor, *N*, is set close to the certified flight envelope limits of the aircraft. In our case these correspond to $N = N_{MAX} = 2.5$ for the pull-up manoeuvres and $N = N_{MIN} = -1$ for the diving manoeuvres. We then assume that during the entire approach to the obstacle, the vehicle control system can provide a linear variation of μ, up to the assumed maximum bank angle. This can be expressed as:

$$\begin{cases} \mu = \mu_0 + \dot{\mu}_{MAX} \cdot t & (\mu \leq \mu_{MAX}) \\ \dot{\mu} = 0 & (\mu = \mu_{MAX}) \end{cases} \quad (2)$$

The maximum roll rate was set at $\dot{\mu}_{MAX} = 20\ °/s$.

5.3 Avoidance geometry

The algorithms for estimation of the obstacle absolute motion based on differential geometry approach were introduced in [20]. In order to provide the fast and reliable performance required for our safety-critical task, the avoidance trajectory generation is based on simplified geometric shapes. The standard deviation of the LOAM detection and tracking error for each axis is given by:

$$\sigma_{(X,Y,Z)} = \sqrt{\sigma^2_{range_{(x,y,z)}} + \sigma^2_{azimuth_{(x,y,z)}} + \sigma^2_{elevation_{(x,y,z)}}} \quad (3)$$

In particular, given the different values of uncertainty associated with the three cardinal directions, an ellipsoidal avoidance volume is implemented in the algorithm. In order to assure adequate safety levels, a separation buffer is introduced, which inflates the ellipsoidal avoidance volume associated with the obstacle. In particular, to provide a confidence level of 95%, the uncertainty associated with the position of an obstacle is calculated as twice the standard deviation (i.e. the two-sigma) of the total obstacle detection and tracking errors. When the distance between two detected obstacles is comparable with the calculated uncertainty values, or with the aircraft dimensions, the algorithm combines the two obstacles in a single avoidance volume. The subsequent step involves the selection of the optimal trajectory from the generated set of safe trajectories, which is then fed to the aircraft guidance subsystems. The implemented decision logic is based on minimisation of the following cost function:

$$J = w_t \cdot t_{SAFE} + w_f \int [SFC \cdot T(t)]dt - w_d \int D(t)dt \quad (4)$$

where t_{SAFE} is the time at the minimum distance point to the obstacle, hence it corresponds to the attainment of a safe condition, $SFC\ [\frac{kg}{N} \cdot s]$ is the specific fuel consumption, $T(t)$ is the thrust profile and $D(t) = \sqrt{\left[\frac{(x(t)-x_{obs})^2}{d^2_{MINx}} + \frac{(y(t)-y_{obs})^2}{d^2_{MINy}} + \frac{(z(t)-z_{obs})^2}{d^2_{MINz}}\right]}$ is the distance from the ellipsoidal avoidance volume of the obstacle. w_t, w_f, w_d are the weightings attributed to time, fuel and integral distance respectively. In time-critical avoidance applications (i.e., closing-up obstacles with high relative velocities and/or accelerations) appropriate higher weightings are used for the time and distance cost elements.

VI. Simulation and Results

Realistic simulation scenarios were implemented to evaluate the avoidance trajectory generation algorithm and assess its performance. The simulation activities were performed on a personal computer with IA64 hardware architecture in realistic three-dimensional scenarios to validate the avoidance trajectory generation algorithm and to assess its performance. The RPAS equipped with LOAM is flying towards a number of obstacles of different geometric characteristics. The original horizontal flight trajectory would lead to a collision. A representative set of avoidance trajectories generated following these assumptions, is depicted in Figure 7. Figure 8 shows the separation envelopes between the aircraft and the boundary surface of the ellipsoidal avoidance volume, calculated for each point of the conflicting and avoidance trajectories.

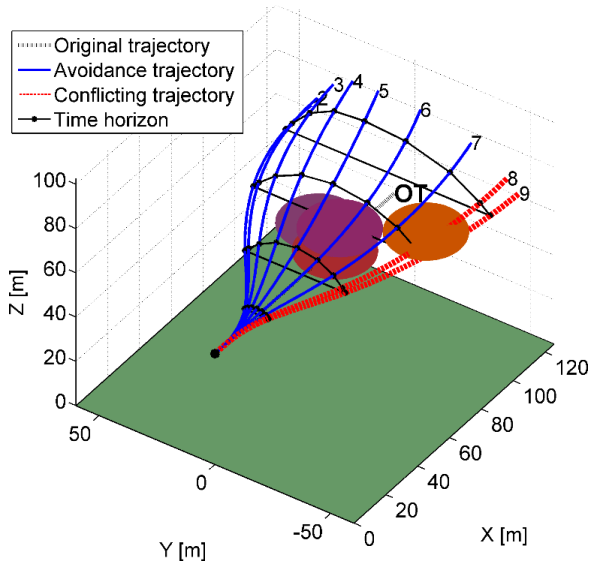

Figure 7. Results of the avoidance trajectory generation algorithm in case of natural obstacles (a) and man-made obstacles (b)

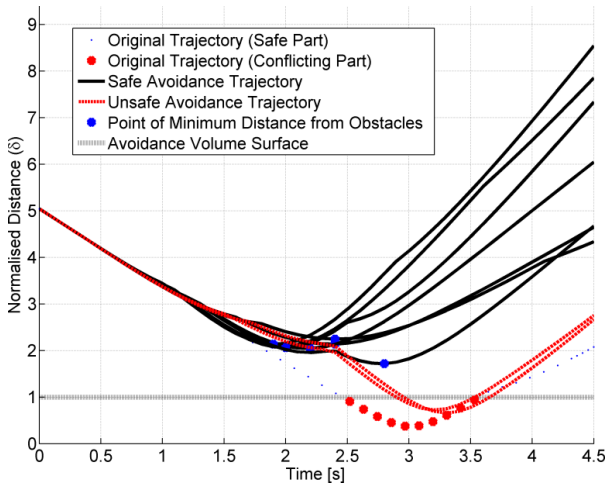

Figure 8. Absolute distance of the generated trajectories from the ellipsoidal avoidance volume boundary

VII. LASER BEAM PROPAGATION

The propagation of laser radiation in atmosphere is affected by a number of linear and nonlinear effects. Assuming a Gaussian profile of the laser beam at the source and an average focused irradiance, the comprehensive expression of the peak irradiance, I_P, accounting for absorption, scattering, diffraction, jitter, atmospheric turbulence and thermal blooming effects is [21]:

$$I_P(z,\lambda) = \frac{b(z)\,\tau(z,\lambda)\,P(\lambda)}{\pi\left(a_d^2(z,\lambda) + a_j^2(z) + a_t^2(z,\lambda)\right)} \quad (5)$$

where z is the linear coordinate along the beam, λ is the wavelength, $P(\lambda)$ is the transmitted laser power, b is the blooming factor, $\tau(z,\lambda)$ is the transmittance coefficient, which accounts for absorption and scattering associated with all molecular and aerosol species present in the path. The 1/e beam radiuses associated with diffraction, $a_d(z,\lambda)$, beam jitter, $a_j(z)$, and turbulence, $a_t(z,\lambda)$, can be calculated as [21, 22]:

$$a_d(z,\lambda) = \frac{Qz\lambda}{2\pi a_0} \quad (6)$$

$$a_j^2(z) = 2\langle\Theta_x^2\rangle\, z^2 \quad (7)$$

$$a_t(z,\lambda) = \frac{2\,C_N^{6/5} z^{8/5}}{\lambda^{1/5}} \quad (8)$$

where Q is the beam quality factor, a_o is the beam *1/e* radius, $\langle\Theta_x^2\rangle$ is the variance of the single axis jitter angle that is assumed to be equal to $\langle\Theta_y^2\rangle$, and C_N^2 is the refractive index structure constant. An empirical model for the blooming factor $b(z)$, which is the ratio of the bloomed I_B to unbloomed I_{UB} peak irradiance, is:

$$b(z) = \frac{I_B}{I_{UB}} = \frac{1}{1 + 0.0625\,N^2(z)} \quad (9)$$

N is the thermal distortion parameter, calculated as:

$$N(z) = \frac{-n_T\,\alpha_m\,P\,z^2}{\pi\,d_0\,v_0\,c_P\,a_0^3} \cdot \left[\frac{2}{z^2}\int_0^R \frac{a_0}{a(z')}dz' \int_0^{z'} \frac{a_0^2\,v_0\,\tau\,''}{a}\,dz''\right] \quad (10)$$

where v_o is the uniform wind velocity in the weak attenuation limit ($\gamma z \ll 1$), n_T , d_o , and c_p are, respectively, the coefficients of index change with respect to temperature, density, and specific heat at constant pressure. The transmittance coefficient τ depends on the integral effect of absorption and scattering phenomena, both for molecular and aerosol species, on the entire beam length, which are comprehensively described as:

$$\tau(z,\lambda) = e^{-\int_0^z \gamma(z,\lambda)\,dz} \quad (11)$$

where $\gamma(z,\lambda)$ is the extinction factor. In the practical case, the molecular and aerosol composition of the atmosphere along the entire LIDAR beam is unknown and cannot be accurately guessed, therefore it is necessary to adopt an empirical model for the extinction factor. Considering that the LIDAR operational wavelength is fixed, and assuming that variations in the transmittance are caused by changes in the water content of the air only, $\gamma(z,\lambda)$ can be calculated using the model suggested by Elder and Strong [23] and modified by Langer [24]. Additionally, for propagation in rainy conditions, the equations developed by Middleton were adopted [25]. This approach (ESLM model) relates the atmospheric transmission of the i^{th} window to the atmospheric visibility, relative humidity and rainfall-rate (i.e., readily measurable parameters). This is a valid assumption since other atmospheric constituents have reasonably constant effects within the given atmospheric window. The number of H_2O molecules encountered by the laser beam can be expressed by the amount of perceptible water, which equals the depth of the layer that would be formed if all the water molecules along the propagation path were condensed in a container having the same cross-sectional area as the beam. Hence, for a beam path length of z meters, the total perceptible water amount in millimetres is:

$$w = 10^{-3}\rho \cdot z \quad (12)$$

where ρ is the absolute humidity [g/m^3]. Two empirical expressions, developed by Langer can be used to calculate the absorptive transmittance τ_{ai} for the i^{th} window for any given value of the perceptible water content [24]. These expressions are:

$$\tau_{ai} = e^{-A_i\sqrt{w}}, \text{ for } w < w_i \quad (13)$$

$$\tau_{ai} = k_i\left(\frac{w_i}{w}\right)^{\beta_i}, \text{ for } w > w_i \quad (14)$$

where A_i, k_i, β_i and w_i are constants whose values for each atmospheric window are listed in [4]. For the LOAM wavelength (λ = 1550 nm - 4th atmospheric window), A_i = 0.211, k_i = 0.802 , β_i = 0.111 and w_i = 1.1. These empirical equations apply to horizontal paths in the atmosphere at sea-level and for varying relative humidity. To obtain the total atmospheric transmittance we must multiply τ_{ai} by τ_{si} (i.e., the transmittance due to scattering only). Based on rigorous mathematical approaches, the scattering properties of the atmosphere due to the aerosol particles are difficult to quantify, and it is difficult to obtain an analytic expression for the scattering coefficient that will yield accurate values over a wide variety of conditions. However, an empirical relationship that is often used to model the scattering coefficient has the form [4]:

$$\beta(\lambda) = C_1\lambda^{-\delta} + C_2\lambda^{-4} \quad (15)$$

where C_1, C_2, and δ are constants determined by the aerosol concentration and size distribution, and λ is the wavelength of the radiation. The second term accounts for *Rayleigh* scattering, which may be neglected for all wavelengths longer than about 0.3 μm. The values $\delta \approx 1.3 \pm 0.3$ produce reasonable results when applied to aerosols with a range of particle sizes. An attempt has also been made to relate δ and C_1 to the meteorological range. The apparent contrast C_z, of a source when viewed at λ = 0.55 μm from a distance z is given by:

$$C_z = \frac{R_{sz} - R_{bz}}{R_{bz}} \quad (16)$$

where R_{sz} and R_{bz} are the apparent radiances of the source and its background as seen from a distance z. For $\lambda = 0.55$ μm, the distance at which the ratio:

$$V = \frac{C_z}{C_0} = \frac{\frac{R_{sz} - R_{bz}}{R_{bz}}}{\frac{R_{s0} - R_{b0}}{R_{b0}}} = 0.02 \tag{17}$$

is defined is termed as the meteorological range V (or visual range). It must be observed that this quantity is different from the *observer visibility* (V_{obs}). Observer visibility is the greatest distance at which it is just possible to see and identify a target with the unaided eye. The International Visibility Code (IVC) designations are too broad for scientific applications. If only an estimated *observer visibility* (V_{obs}) is available, the meteorological range (V) can be estimated from [4]:

$$V \approx (1.3 \pm 0.3) \cdot V_{obs} \tag{18}$$

Assuming that the source radiance is much greater than the background radiance (i.e., $R_s >> R_b$) and that the background radiance is constant (i.e., $R_{bo} = R_{bz}$), then the transmittance at λ = 0.55 μm (where absorption is negligible) is given by:

$$\frac{R_{sv}}{R_{s0}} = e^{-\beta V} = 0.02 \tag{19}$$

Hence, we have:

$$\ln\left(\frac{R_{sv}}{R_{s0}}\right) = -\beta V = -3.91 \tag{20}$$

and also:

$$\beta = \frac{3.91}{V} = C_1 \lambda^{-\delta} \tag{21}$$

The constant C_1 is given by:

$$C_1 = \frac{3.91}{V} \cdot 0.55^{\delta} \tag{22}$$

With this result the transmittance at the centre of the i^{th} window is:

$$\tau_{si} = e^{-\frac{3.91}{V}\left(\frac{\lambda_i}{0.55}\right)^{-\delta} \cdot z} \tag{23}$$

where λ_i must be expressed in microns. If, because of haze, the meteorological range is less than 6 km, the exponent δ is related to the meteorological range by the following empirical formula:

$$\delta = 0.585\sqrt[3]{V} \tag{24}$$

where V is in kilometres. When $V \geq 6$ km, the exponent δ can be calculated by:

$$\delta = 0.0057 \cdot V + 1.025 \tag{25}$$

For exceptionally good visibility δ = 1.6, and for average visibility $\delta \approx 1.3$. In summary, an appropriate value for δ allows to compute the scattering transmittance at the centre of the i^{th} window for any propagation path, if the meteorological range V is known. During periods of high humidity, water molecules condense onto microscopic particles such as salt crystals, very fine dust, and combustion products, whose initial radii of less than 0.5 μm increase in size. Since salt is quite hygroscopic, it is by far the most important condensation nucleus. Fog occurs when the condensation nuclei grow into water droplets or ice crystals with radii exceeding 0.5 μm. By convention fog limits the visibility to less than 1 km, whereas in a mist the visibility is greater than 1 km. We know that in the early stages of droplet growth the Mie attenuation factor K depends strongly on the wavelength. When the drop has reached a radius $a \approx 10 \cdot \lambda$ the value of K approaches 2, and the scattering is now independent of wavelength, i.e., it is non-selective. Since most of the fog droplets have radii ranging from 5 to 15 μm they are comparable in size to the wavelength of infrared radiation. Consequently the value of the scattering cross section is near its maximum. It follows that the transmission of fog in either the visible or *IR* spectral region is poor for any reasonable path length. This of course also applies to clouds. Since haze particles are usually less than 0.5 μm, we note that for laser beams in the *IR* spectral region $a/\lambda \ll 1$ and the scattering is not an important attenuation mechanism. This explains why photographs of distant objects are sometimes made with infrared-sensitive film that responds to wavelengths out to about 0.85 μm. At this wavelength the transmittance of a light haze is about twice that at 0.5 μm. Raindrops are of course many times larger than the wavelengths of laser beams. As a result there is no wavelength-dependent scattering. The scattering coefficient does, however, depend strongly on the size of the drop. The scattering coefficient with rain is approximated by [25]:

$$\beta_{rain} = 1.25 \cdot 10^{-6} \frac{\Delta x / \Delta t}{a^3} \tag{26}$$

where $\Delta x/\Delta t$ is the rainfall rate in centimetres of depth per second and a is the radius of the drops in centimetres. In order to obtain accurate estimates, the distribution of raindrop sizes and the associated rainfall rates should be known. In this case, the scattering coefficient can be calculated as the sum of the partial coefficients associated to the various raindrops. A simpler approach, used in LOWTRAN, gives good approximations of the results obtained for most concentrations of different rain particles. Particularly, in LOWTRAN, the scattering coefficient with rain has been empirically related only to the rainfall rate $\Delta x/\Delta t$ (expressed in mm/hour), as follows:

$$\beta_{rain} \approx 0.365 \cdot \left(\frac{\Delta x}{\Delta t}\right)^{0.63} \tag{27}$$

Table 2 provides representative rainfall rates which can be used in eq. (23) and (24), when no direct measurements are available, to obtain order of magnitude estimations of β_{rain}.

TABLE III. REPRESENTATIVE RAINFALL RATES

Rain Intensity	Rainfall (mm/hour)
Mist	0.025
Drizzle	0.25
Light	1.0
Moderate	4.0
Heavy	16
Thundershower	40
Cloud-burst	100

In the presence of rain, in addition to the scattering losses calculated with eq. (27) or (28), there are also losses by absorption along the path, and these must be included in the calculation of the total atmospheric transmittance with rain. In order to estimate the SNR from experimental LOAM detector current measurements (i_{SIG}), obtained with certain obstacle ranges (R) and incidence angles (θ), SNR is expressed as follows:

$$SNR = 20\log\left[\frac{i_{SIG}(R,\theta)}{i_{NOISE}}\right] \tag{28}$$

The noise current term in eq. (25) is modelled as:

$$i_{NOISE} = \sqrt{i_{TH}^{\ 2} + i_{BK}^{\ 2} + i_{DK}^{\ 2} + i_{RA}^{\ 2}} \tag{29}$$

where i_{TH} is the thermal noise current, i_{BK} is the background noise current, i_{DK} is the dark noise current and i_{RA} is the receiver amplifier noise. According to the LOAM design characteristics, we have:

$$i_{BK} = \sqrt{2qP_S P_h M_A (2 + kM_A)B} \tag{30}$$

$$i_{TH} = \sqrt{4K_B \frac{T_k Bk}{R_L}} \tag{31}$$

$$i_{DK} = 0.5 \cdot 10^{-12} \tag{32}$$

$$i_{RA} = 1.5 \cdot 10^{-12} \tag{33}$$

where:

P_S = received solar power
P_h = amplifier gain
M_A = avalanche multiplier
k = noise factor of the avalanche photodiode
B = electronic bandwidth
K_B = Boltzmann constant (1.39×10-23 J/°K)
T_k = absolute temperature (°K)
R_L = amplifier load resistance

The following characteristics were defined for a wire type obstacle according to LOAM operational requirements:

- Diameter: 5 mm ≤ D_W ≤ 70 mm
- Shape: twisted or round
- Reflection: Purely diffuse (Lambertian)
- Reflectivity: ≥ 20% (θ = 0)

The reference environmental parameters were set as follows:

- Visibility: V ≥ 800 m
- Humidity: RH ≤ 100%
- Temperature: T ≤ 50 °C
- Rain: Light/Medium/Heavy
- Background: P_B = 50 W/m2 sr μm

For calculation purposes, the i_{SIG} (R,θ) term is modelled as:

$$i_{SIG} = \sqrt{\frac{P_T d_W \rho D_a^{\ 3} \eta e^{-2\gamma R}}{4R^3 \lambda} \cdot \frac{P_h}{K_a} \cdot \frac{1}{R_L}} \tag{34}$$

where P_T is transmitted power, P_h is amplifier gain, D_a is aperture diameter and K_a is aperture illumination constant = $\sin(\theta)^{5.4}$ .The false alarm probability is modelled as [26]:

$$P_{fa} = \frac{1}{B \cdot T_{fa} \cdot \eta} \tag{35}$$

where B is receiver bandwidth, T_{fa} is mean time between false alarms and η is the maximum useful/non-ambiguous range. The mean time between false alarms corresponds to elementary electrical false alarm at the receiver level. The probability to have several false alarms on a straight line pattern is significantly lower. Statistically, these phenomena are described by the False Alarm Rate (FAR) and Detection Probability (P_d). If the noise and signal distributions are known, the SNR can be estimated and the corresponding D_P and FAR can be determined. According to the Rice calculation [26], the average FAR for the LOAM system is given by:

$$\overline{FAR} = \frac{1}{2\tau\sqrt{3}} \exp\left(-\frac{I_t^2}{2I_n^2}\right) \tag{36}$$

where τ is the electrical pulse length, I_t is the threshold current and I_n is the average noise current. The LOAM P_d is determined using pure Gaussian statistics:

$$P_d = \frac{1}{\sqrt{\pi}} \int_{\frac{I_t - I_n}{\sqrt{2}I_n}}^{\infty} \exp\left(-\frac{i_n^2}{2I_n^2}\right) d\left(\frac{i_n}{\sqrt{2}I_n}\right) \tag{37}$$

where I_n is the average signal current and i_n is the instantaneous noise current. The false alarm probability (P_{fa}) is therefore given by:

$$P_{fa} = \tau \cdot \overline{FAR} \tag{38}$$

and the cumulative detection probability (P_D) is given by:

$$P_D = 1 - \sum_{i=0}^{m} C_M^i P_d^i (1 - P_d)^{M-i} \tag{39}$$

where M is number of possible detections and m is minimum number of detections required. The performance estimation models introduced in this section enable the extension of the collected ground and flight test results to all the platform maneuvering envelopes.

VIII. HUMAN-MACHINE INTERFACE AND INTERACTION (HMI^2)

In low integration architectures, information relative to all detected obstacles is provided on a dedicated avionic display. Both 3D and 2D display formats are available, as well as an altimetry display format. Figure 9 shows a visible image (a) and the corresponding LOAM 3D display format (b). Comparing Figure 9 (a) and (b), it is evident that poles and wire obstacles placed at a certain distance from the platform and hard to be seen by a visual camera (and by the human eye) are successfully detected and displayed by the LOAM. A 2D display format is also available (Figure 9 (c)) as well as a combined format, shown in Figure 9 (d), providing a synthetic augmented-reality image of the scene captured by the visual camera and by the LOAM.

(a)

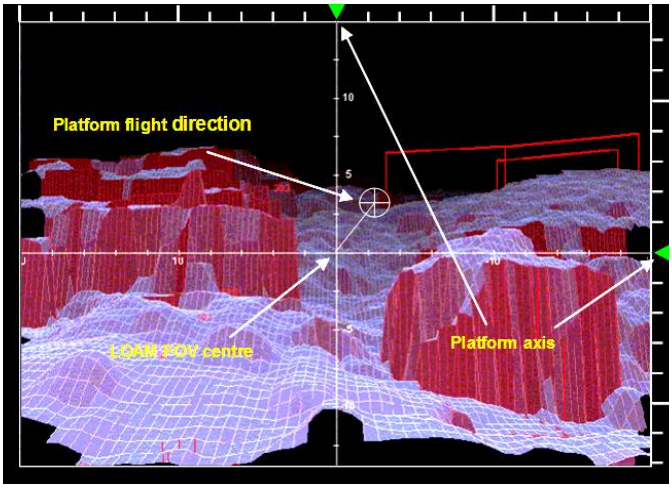

(b)

(c)

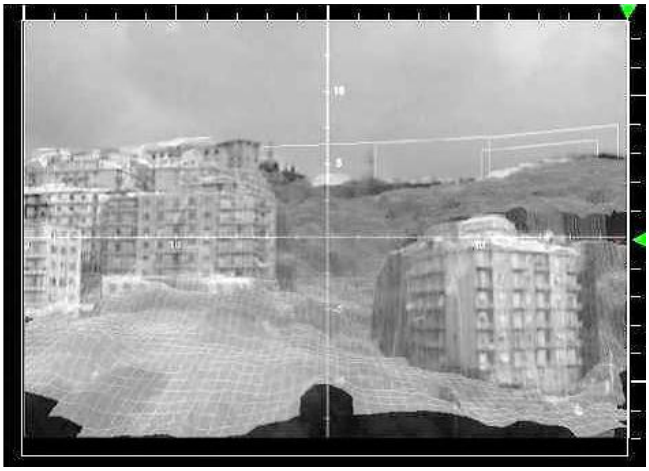

(d)

Figure 9. Visible camera image (a), LOAM 3D display (b), 2D display (c) and synthetic enhanced-reality image (d).

An altimetry display format is also available and depicted in Figure 10. In all these avionics implementations, the actual platform orientation and velocity vector flight path with respect to the LOAM axis are represented (an auto-alignment function can be also implemented if the required data are available from other avionics navigation and guidance systems).

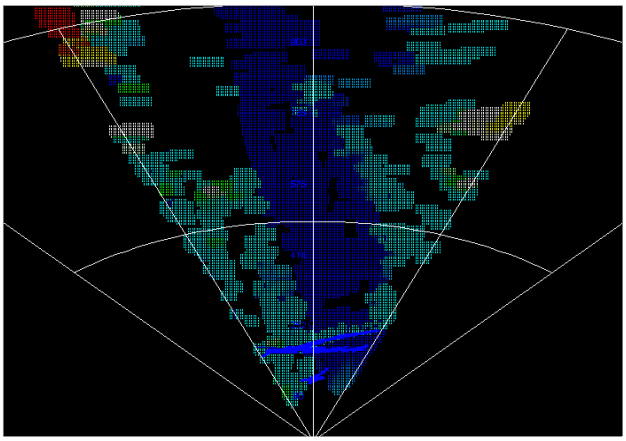

Figure 10. LOAM altimetry display formats.

IX. GROUND TESTING

Ground trials of the LOAM were performed in order to estimate the system detection performance in various weather and obstacle conditions to test the validity of the mathematical models used for performance calculations [4, 27, 28]. In particular ground tests were performed in various weather conditions (i.e., clear weather with $10 \leq V \leq 15$ km, and light/medium/heavy rain), using a wire of known section and reflectivity (D_W = 2.5 cm and ρ = 40%). The sets of data collected in clear and rainy weather conditions were obtained. Form these data, it was evidenced that the returned signal power fluctuates independently from pulse to pulse according to a Gaussian distribution. A comparison between the SNR predicted (SNR_P) with γ calculated using the ESLM model ($0.19\ km^{-1} \leq \gamma \leq 0.22\ km^{-1}$ for clear weather and $1.23\ km^{-1} \leq \gamma \leq 2.94\ km^{-1}$ for rainy conditions), assuming a background power of 10 Watt/m^2/sr/μm and ρ = 0.5, and estimated from experimental data (SNR_E), is shown in Table 3.

TABLE IV. LOAM PREDICTED AND MEASURED SNR'S.

	Clear Weather			Rain		
	V = 10 km	V = 12.5 km	V = 15 km	Light	Medium	Heavy
SNR_P	4.90×10^4	4.95×10^4	5.02×10^4	3.14×10^4	1.83×10^4	1.45×10^4
SNR_E	3.35×10^4	3.80×10^4	4.27×10^4	2.87×10^4	2.47×10^4	2.13×10^4

X. PROTOTYPE FLIGHT TEST ACTIVITIES

The extensive flight test activities performed have addressed, in particular, the Human-Machine Interface and Interaction (HMI^2) and avoidance trajectory generation algorithms for rotorcraft low-level flight. Two different rotorcraft platforms were used for these tests: NH-300 and AB-212. For the AB-212 test campaign, the LOAM MCU was installed in the centre of the pedestal console, in a position accessible to both pilot and co-pilot. During the test flights, a Flight Test Engineer operated a computer, linked to the LOAM system and displaying in real-time a 3D image reconstructed using the LOAM data. All images were recorded for the successive data analysis. The results of this test campaign were very satisfactory. Particularly, the LOAM range performances were in accordance with the predictions and the LOAM detection/classification algorithms were validated. Furthermore, it was verified that the LOAM history function was adequate to cover the flight envelope of the selected test platforms. Table 4 shows the detection range results obtained for wire obstacles of 5 mm in diameter, in dry weather (visibilities of 800 m, 1500 m and 2000 m), and incidence angles of 90° and 45°. It is evident that LOAM fulfils the minimum performance requirements set for the designated rotorcraft platforms. The experimental detection ranges also exceed the ESLM model detection ranges and this is due to a slight overestimation of the extinction coefficient at λ=1.55μm as detailed in [11].

TABLE V. DETECTION RANGE OF 5 MM DIAMETER CABLE.

Visibility	Incidence Angle	ESLM Model Det. Distance	Actual Det. Distance	Minimum Specified Det. Distance
800 m	90°	662 m	727 m	500 m
1500 m	90°	783 m	832 m	560m
2000 m	90°	921 m	980 m	600 m
800 m	45°	495 m	529 m	400 m
1500 m	45°	553 m	623 m	440 m
2000 m	45°	629 m	657 m	520 m

XI. FUTURE DEVELOPMENT AND TEST ACTIVITIES

The candidate platforms for LOAM integration and flight test activities include the AB412, A129, NH90 and EH101 rotorcraft, as well as various fixed and rotary wing RPAS platforms (Figure 11).

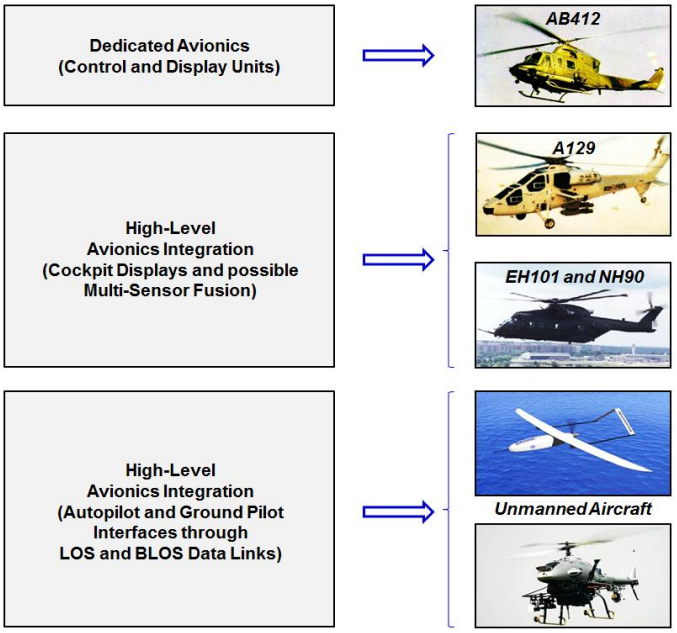

Figure 11. Candidate platforms for LOAM integration.

For small-size RPAS, a scaled version of the LOAM, currently under development, is conceived for integration in the forward section of the RPAS by removing the chassis and tailoring the design of the various optical and electronic components for this application [20, 29]. Error analysis is performed to determine the overall uncertainty volume in the airspace surrounding the intruder track based on Sabatini-Ramasamy Unified Method (SUM) [29]. A dedicated LOAM control unit is also being developed for RPAS applications. Its characteristics are conceptually similar to the MCU developed for the initial rotorcraft flights. However, as this MCU is to be operated by the remote pilot, in this case the LOAM operating modes are activated using two different communication data links for Line-of-Sight (LOS) and Beyond LOS (BLOS)

operations. Additionally, the LOAM display functions are planned to be integrated in the RPS and the required LOAM display formats displayed to the RPAS pilot in real-time. Specific activities will address the integration of LOAM with Forward Looking Infrared (FLIR) and Night Vision Imaging Systems (NVIS), in order to investigate the synergies attainable in terms of obstacle/threat detection, recognition and identification [30-32]. In higher-level integration layouts (e.g., EH101, NH90, AB129 and RPAS), the LOAM obstacle information and the computed optimal avoidance flight path data are provided to the flight crew in a synthetic form using the avionics Multi-Function Displays (MFD) in the flight deck (case of rotorcraft) or in the Remote Piloting Station (RPS) displays (case of RPAS). The potential interfaces between LOAM and other avionics and Air Traffic Management (ATM) systems are also being investigated. In particular, current research is addressing the possible direct integration of LOAM and other Forward-Looking Sensors (FLS) information with manned aircraft and RPAS Guidance, Navigation and Control (GNC) systems [33, 34], and with the next generation of Air Traffic Management (ATM) systems being conceived for 4D Trajectory Based Operations (TBO) [35, 36]. Figure 12 shows the synthetic display formats currently being developed for the RPAS displays. In particular, Figure 12 (a) depicts the safety line, which connects the points of minimum pitch for safe obstacle avoidance at all azimuths. Figure 12 (b) illustrates the representation of wire and pole-shaped obstacles, whereas Figure 12 (c) shows obstacles of all obstacles including the ones with bulk geometry (trees). Figure 12 (d) depicts the synthetic vision format integrating information from the LOAM and from FLIR systems.

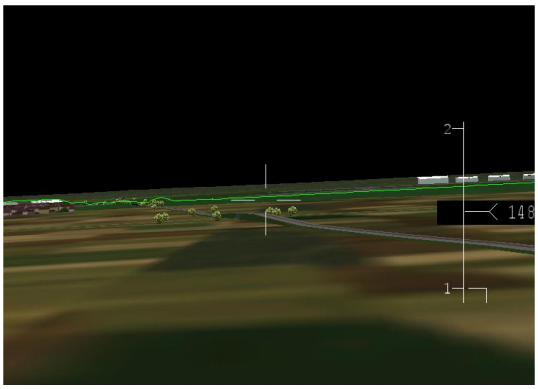

(a)

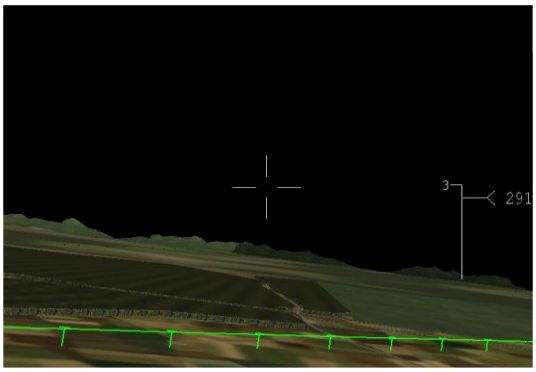

(b)

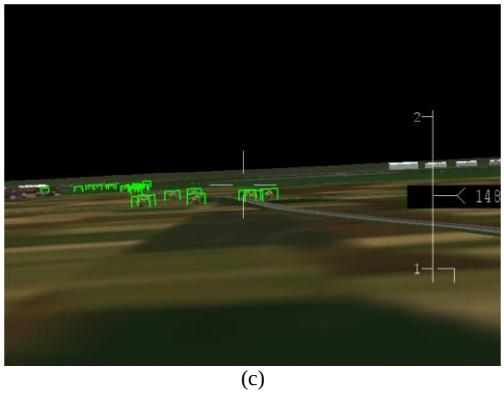

(c)

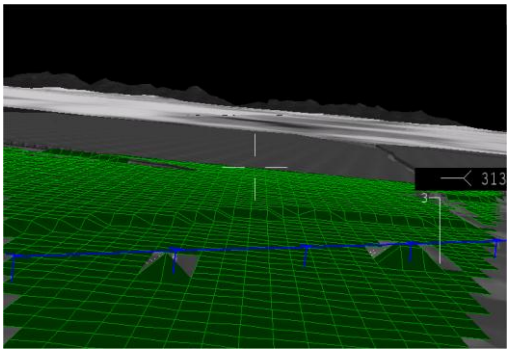

(d)

Figure 12. Synthetic display formats: safety line (a), wires and poles (b), all obstacles (c) and integrated LOAM/FLIR (d)

XII. ACKNOWLEDGEMENTS

This activity was partly funded by the Italian Ministry of Defence (MoD) under R&D contract No. 2097-22-12-2000. The Italian Air Force Flight Test Centre developed the mathematical models, simulation tools and test facilities required for system ground and flight test. The authors wish to thank the personnel of SELEX-ES, LOT-ORIEL and the Italian MoD Laser Test Range (PILASTER) for helping in the preparation and execution of the ground and flight test activities.

REFERENCES

[1] J. Lai, J. J. Ford, L. Mejias, P. O'Shea, and R. Walker, "See and Avoid Using Onboard Computer Vision", pp. 265-294, John Wiley and Sons, 2012.

[2] S. I. Ali Shah and E. N. Johnson, "3D obstacle detection using a single camera", in proceedings of AIAA Guidance, Navigation, and Control conference 2009 (GNC 2009), Chicago, IL, USA, 2009

[3] J. Gauci and D. Zammit-Mangion, "Obstacle detection around aircraft on ramps and taxiways through the use of computer vision", in proceedings of AIAA Guidance, Navigation, and Control Conference (GNC 2009), Chicago, IL, USA, 2009

[4] R. Sabatini and M. A. Richardson, Airborne Laser Systems Testing and Analysis, RTO AGARDograph AG-300 Vol. 26, Flight Test Instrumentation Series, Systems Concepts and Integration Panel (SCI-126) vol. RTO AGARDograph AG-300 Vol. 26, NATO Science and Technology Organization, 2010.

[5] M. J. Kochenderfer, L. P. Espindle, J. D. Griffith, and J. K. Kuchar, "Encounter modeling for sense and avoid development", in proceedings of 2008 Integrated Communications, Navigation and Surveillance Conference (ICNS 2008), Bethesda, MD, USA, 2008. DOI: 10.1109/ICNSURV.2008.4559177

[6] K. R. Noth, "Modeling and simulation of a ground based sense and avoid architecture for Unmanned Aircraft System operations", in proceedings of 11th Integrated Communications, Navigation and Surveillance Conference: Renovating the Global Air Transportation System (ICNS 2011), Herndon, VA, USA, 2011, pp. O71-O79. DOI: 10.1109/ICNSURV.2011.5935356

[7] R. Carnie, R. Walker, and P. Corke, "Image processing algorithms for UAV "sense and avoid"", in proceedings of 2006 IEEE International Conference on Robotics and Automation (ICRA 2006), Orlando, FL, USA, 2006, pp. 2848-2853. DOI: 10.1109/ROBOT.2006.1642133

[8] C. B. Kellington, "An optical radar system for obstacle avoidance and terrain following", in AGARD-CP-148, NATO Science and Technology Organization, 1965.

[9] B. S. Goldstein and G. F. Dalrymple, "Gallium arsenide injection laser radar", Proceedings of the IEEE, vol. 55, pp. 181-188, 1967. DOI: 10.1109/proc.1967.5437

[10] R. Sabatini and M. A. Richardson, "A new approach to eye-safety analysis for airborne laser systems flight test and training operations", Optics and Laser Technology, vol. 35, pp. 191-198, 2003. DOI: 10.1016/S0030-3992(02)00171-8

[11] R. Sabatini, M. A. Richardson, H. Jia, and D. Zammit-Mangion, "Airborne laser systems for atmospheric sounding in the near infrared", in proceedings of SPIE 8433, Laser Sources and Applications, Photonics Europe 2012, Brussels, Belgium, 2012. DOI: 10.1117/12.915718

[12] G. Hogg, K. Harrison, and S. Minisclou, "The Anglo-French Compact Laser Radar Demonstrator Programme", in AGARD-CP-563 - Low-Level and Nap-of-the-Earth (NOE) Night Operations, NATO Science and Technology Organization, 1995.

[13] W. Büchtemann and M. Eibert, "Laser based obstacle warning sensors for helicopters", in AGARD-CP-563 - Low-Level and Nap-of-the-Earth (NOE) Night Operations, vol. CP-563, NATO Science and Technology Organization, 1994.

[14] S. L. Holder and R. G. Branigan, "Development and Flight Testing of an Obstacle Avoidance System for the US Army Helicopters", in AGARD-CP-563 - Low-Level and Nap-of-the-Earth (NOE) Night Operations, vol. CP-563, NATO Science and Technology Organization, 1994.

[15] R. Sabatini, E. Roviaro, and M. Cottalasso, "Development of a Laser Collision Avoidance System for Helicopters: Obstacle Detection/Classification and Calculation of Alternative Flight Paths", in RTO-MP-092 - Complementarity of Ladar and Radar, NATO Research and Technology Organization (RTO), 2002.

[16] R. Sabatini, A. Gardi, S. Ramasamy, and M. A. Richardson, "A Laser Obstacle Warning and Avoidance System for Manned and Unmanned Aircraft", in proceedings of IEEE Metrology for Aerospace (MetroAeroSpace 2014), Benevento, Italy, 2014, pp. 616-621. DOI: 10.1109/MetroAeroSpace.2014.6865998

[17] R. Sabatini, A. Gardi, and M. A. Richardson, "LIDAR Obstacle Warning and Avoidance System for Unmanned Aircraft", International Journal of Mechanical, Aerospace, Industrial and Mechatronics Engineering, vol. 8, pp. 62-73, 2014

[18] M. Cottalasso, "EP 2 175 303 A1 - Laser Scanning Device", European Union Patent, 2010.

[19] M. Burston, R. Sabatini, A. Gardi, and R. Clothier, "Reverse Engineering of a Fixed Wing Unmanned Aircraft 6-DoF Model Based on Laser Scanner Measurements", in proceedings of IEEE Metrology for Aerospace (MetroAeroSpace) 2014, Benevento, Itay, 2014. DOI: 10.1109/MetroAeroSpace.2014.6865910

[20] L. Rodriguez Salazar, R. Sabatini, A. Gardi, and S. Ramasamy, "A Novel System for Non-Cooperative UAV Sense-and-Avoid", in proceedings of European Navigation Conference 2013 (ENC2013), Vienna, Austria, 2013

[21] F. G. Gebhardt, "High Power Laser Propagation", Applied Optics, vol. 15, pp. 1479-1493, 1976

[22] R. Sabatini and M. A. Richardson, RTO AGARDograph AG-300 Vol. 26: Airborne Laser Systems Testing and Analysis, Systems Concepts and Integration Panel (SCI-126), NATO Science and Technology Organization, 2010.

[23] T. Elder and J. Strong, "The infrared transmission of atmospheric windows", Journal of the Franklin Institute, vol. 255, pp. 189-208, 1953

[24] R. M. Langer, "Report on Signal Corps Contract No. DA-36-039-SC-72351", 1957.

[25] W. E. K. Middleton, "Vision through the Atmosphere", University of Toronto Press, 1952.

[26] M. I. Skolnik, Radar handbook, 1970.

[27] R. Sabatini and M. A. Richardson, "Airborne Laser Systems Testing, Safety Analysis, Modelling and Simulation", presented at the 21st Annual Symposium of the Society of Flight Test Engineers - European Chapter, Vergiate (VA), Italy, 2010.

[28] R. Sabatini and M. A. Richardson, "Novel atmospheric extinction measurement techniques for aerospace laser system applications", Infrared Physics and Technology, vol. 56, pp. 30-50, 2013. DOI: 10.1016/j.infrared.2012.10.002

[29] S. Ramasamy, R. Sabatini and A. Gardi, "Towards a Unified Approach to Cooperative and Non-Cooperative RPAS Detect-and-Avoid", Fourth Australasian Unmanned Systems Conference 2014 (ACUS 2014), Melbourne, Australia. DOI: 10.13140/2.1.4841.3764

[30] R. Sabatini, M. A. Richardson, M. Cantiello, M. Toscano, and P. Fiorini, "A novel approach to night vision imaging systems development, integration and verification in military aircraft", Aerospace Science and Technology, 2013. DOI: 10.1016/j.ast.2013.08.021

[31] R. Sabatini, M. A. Richardson, M. Cantiello, M. Toscano, P. Fiorini, H. Jia, et al., "Night Vision Imaging Systems design, integration and verification in military fighter aircraft", in proceedings of SPIE 8439, Optical Sensing and Detection II, Photonics Europe 2012, Brussels, Belgium, 2012. DOI: 10.1117/12.915720

[32] R. Sabatini, M. A. Richardson, M. Cantiello, M. Toscano, P. Fiorini, D. Zammit-Mangion, et al., "Experimental flight testing of night vision imaging systems in military fighter aircraft", Journal of Testing and Evaluation, vol. 42, 2014. DOI: 10.1520/JTE20120339

[33] S. Ramasamy, R. Sabatini, A. Gardi, and Y. Liu, "Novel flight management system for real-time 4-dimensional trajectory based operations", in proceedings of AIAA Guidance, Navigation, and Control Conference 2013 (GNC 2013), Boston, MA, USA, 2013. DOI: 10.2514/6.2013-4763

[34] S. Ramasamy, R. Sabatini, A. Gardi, and T. Kistan, "Next Generation Flight Management System for Real-Time Trajectory Based Operations", Applied Mechanics and Materials, vol. 629, pp. 344-349, 2014. DOI: 10.4028/www.scientific.net/AMM.629.344

[35] A. Gardi, R. Sabatini, S. Ramasamy, and K. de Ridder, "4-Dimensional Trajectory Negotiation and Validation System for the Next Generation Air Traffic Management", in proceedings of AIAA Guidance, Navigation, and Control Conference 2013 (GNC 2013), Boston, MA, USA, 2013. DOI: 10.2514/6.2013-4893

[36] A. Gardi, R. Sabatini, S. Ramasamy, and T. Kistan, "Real-Time Trajectory Optimisation Models for Next Generation Air Traffic Management Systems", Applied Mechanics and Materials, vol. 629, pp. 327-332, 2014. DOI: 10.4028/www.scientific.net/AMM.629.327